

LASER GYROSCOPES

PACS numbers: 06.30.Gv; 07.07.Df; 07.60.Ly
DOI: 10.1070/QE2015v045n01ABEH015420

Precise laser gyroscope for autonomous inertial navigation

A.G. Kuznetsov, A.V. Molchanov, M.V. Chirkin, E.A. Izmailov

Abstract. **Requirements to gyroscopes of strapdown inertial navigation systems for aircraft application are formulated. The construction of a ring helium–neon laser designed for autonomous navigation is described. The processes that determine the laser service life and the relation between the random error of the angular velocity measurement and the surface relief features of the cavity mirrors are analysed. The results of modelling one of the promising approaches to processing the laser gyroscope signals are presented.**

Keywords: *laser gyroscope, ring laser, autonomous inertial navigation, lock-in threshold, reactive oscillations, cathode sputtering, backscattering, forced dithering, quadrature signals, quantisation noise.*

1. Peculiarities of using a laser gyroscope in aircraft autonomous inertial navigation

The effectiveness of the flight task execution by mobile facilities is determined by the assemblage of on-board systems and complexes, including the equipment providing the arrival at the prescribed region and the reliable functioning of a control and guidance systems, mounted directly aboard the mobile facility. This stimulated the development of on-board navigation systems based on different physical principles. The use of passive systems essentially reduces the possibility of the object detection due to the absence of radiation sources aboard. However, most of them, including the satellite navigation system, are subjected to disturbances, which, obviously, is not favourable for the solution of the formulated problem. The inertial navigation systems (INS's) are those that fit the requirements of autonomy and noise protection most completely.

The development of INS's, mainly for aircraft application, was started at the Moscow Institute of Electromechanics and Automatics as far back as in the 1960s. By the end of the 1990s the Institute had developed several modifications of platform inertial navigation systems (PINS's) based on fluid-suspended astatic gyroscopes, which are in exploitation even now. Aircrafts Su-24, Tu-22M, Tu-142M and Tu-95MS employ MIS-45, MIS-P and L-14MA systems developed in the 1960s–1970s and aircrafts Il-76, Tu-154M, Tu-160, An-124 and An-225 make use of I-11-1, I-21 and L-41 systems (1980s). However, the presence of complex mechanics and follower drivers of the cardan joint suspension limits the potential development of PINS's aimed at reducing cost and energy consumption, at increasing operation lifetime, reliability and informativity and at reducing maintenance expenses.

In the 1970s intense studies aimed at the development of strapdown inertial navigation system (SINS) were started all over the world. At present, the world trends of INS development are associated with practically complete transition to the SINS ideology [1–4]. In comparison with platform systems they possess 3–4 times greater informativity, 1.5–3 times shorter autonomous initial alignment time, 2–3 times smaller overall dimensions and mass, 10 times smaller energy consumption and 10 times greater useful service time, which reduces the cost of the life cycle by orders of magnitude [5]. The specificity of the systems of this type consists in rigid connection of the unit of inertial sensitive elements (SEs) to the axes of the object, i.e., in the replacement of the physical platform with the mathematical one, which is the basis of all technical requirements to the gyroscopic SEs independent of their type.

A real platform allows the calibration of SEs, their horizontal alignment and physical orientation of the platform axes by double gyrocompassing at each switch-on of the system. The mathematical platform excludes the possibility of implementing these procedures. The initial alignment error of SINS's is determined not only by the starting instability of drift characteristics of the SEs but also by their instability from start to start and by the instability of the gyroscope scale coefficient [5, 6].

In the navigation regime, the SINS gyroscope plays the role of a zero indicator in the case of using the inertial coordinate system or the positioner of small angular velocity of the Earth fly-around for supporting the local vertical in the geographic coordinate system. The dynamic range of the object angular velocity is compensated for by the follower system of the platform cardan suspension. Hence, there are no requirements to the gyroscope concerning the wide dynamic range and high stability of the scale coefficient within its limits. In the case of the mathematical platform the above requirements are equivalent to the requirements of the SE drift characteristics stability, since they directly affect the system error in the navigation regime. The reduction of energy consumption and the precision readiness time unambiguously implies the elimination of SE thermal stabilisation systems. The introduction of algorithmic compensation for temperature dependences of the SE parameters imposes severe requirements on their stability [7].

A.G. Kuznetsov, A.V. Molchanov, E.A. Izmailov JSC 'Moscow Institute of Electromechanics and Automatics (MIEA)', Aviatsionnyi pereulok 5, 125319 Moscow, Russia; e-mail: aomiea@aviapribor.ru, a.v.molchanov@mail.ru;
M.V. Chirkin Ryazan State Radio Engineering University, ul. Gagarina 59/1, 390005 Ryazan, Russia; e-mail: chirk.mikhail@yandex.ru

Received 25 January 2014; revision received 30 April 2014
Kvantovaya Elektronika **45** (1) 78–88 (2015)
Translated by V.L. Derbov

Table 1. Development of SINS's based on laser gyroscopes at the JSC 'MIEA'.

System	Basic device	Parameters			Aircraft
		Accuracy/km h^{-1}	Mass/kg	Readiness/min	
1st generation (1990–2000)					
I42-1S	Laser gyroscope KM-11-1A ('Polus')	3.7	43	15	Il-96-300, Tu-204, An-70
SINS-85 SINS-77	Laser gyroscope LG-1 (JSC 'MIEA')	3.7	20	10	
2nd generation (2000–2010)					
SINS-SP-1	Block of laser gyroscopes BLG (JSC 'MIEA')	3.7	15	5	Yak-130, Su-35, Tu-160M, Tu-95MSM, T-50
SINS-SP-2		1.85	15	5	
3rd generation (since 2010)					
SINS-21	Block of digital laser gyroscopes BLG (JSC 'MIEA')	0.9	15	4	PAK FA, PAK DA

The implementation of the above characteristics in conventional gyroscopes proved practically impossible, making it necessary to find principally new gyroscopic technologies. At present, laser gyroscope (LG) technology has become widely used in the world as the one providing the most complete fulfilment of all requirements [8]. In accordance with the world trends of the avionics development, in 1984–1991 at the JSC 'MIEA' the first domestic SINS's for aircraft application, I-41-1S, was created on the basis of a KM-11-1A laser gyroscope (M.F. Stelmalkh 'Polus' Research and Development Institute), which was installed aboard Il-96 and Tu-204 aircrafts and manufactured serially for several years.

During those years it was decided to start the development and pilot production of LGs, more completely satisfying the requirements necessary for aircraft SINS's. The LG-1 gyroscope was developed, and on its basis, BINS-77 and BINS-85 systems were designed for military transport airplanes and civil aircrafts, respectively. These systems passed all tests and were certified by the IAC as ready to be installed on aircrafts [9]. These systems became a basis for further development of the line of modern BINS-SP-1 and BINS-SP-2 systems used on the manoeuvre aircrafts Yak-130, Su-35S and in future – on T-50 (Table 1).

The developed LG technology with forced dithering and planar ray contour is oriented at the requirements of aircraft application: dynamic range of angular velocity measurements up to 400 deg s^{-1}, relative error of the scale factor no greater than 10^{-6}, precision readiness time no greater than 10 s, temperature range from –60 °C to +85 °C and minimal possible energy consumption, mass and overall dimensions. However, the used methods of information signal processing [10] and the devices for their implementation suffer from a number of essential drawbacks, such as a high level of fluctuations in the output signal associated with the use of chaotically modulated dithering frequency and quantisation noise, the appearance of additional errors caused by the subtracting of the parameters of ring laser oscillations at the dithering frequency from the output data, the necessity of using auxiliary devices intended for the control and correction of the LG operation.

Depending on the accuracy class of the system, the total error of the gyroscope, including the starting instability and the irreproducibility from start to start, the temperature drift coefficient and the noise component of the drift, should not exceed the values summarised in Table 2 [11]. The systems of the third and second accuracy class are already designed, and at present the problem to be solved is to construct a system of the first accuracy class, oriented at the solution of navigation problems in promising front-line aviation aircraft complexes (PAK FA) and long-range future aviation complexes for Strategic Air Forces (PAK DA) (see Table 1).

Table 2. SINS accuracy classes.

SINS accuracy class	Error of coordinate determination (2σ) during 1 h/km	Gyroscope error/deg h^{-1}	Noise component of drift/deg $h^{-1/2}$
1	0.9	0.005	0.001
2	1.85	0.008	0.0015
3	3.7	0.015	0.003

In the present paper we analyse the potential capabilities of improving the LG technology with forced dithering and planar ray contour in relation to providing the ring laser operability during tens of thousand hours of continuous operation, metrological approaches to the monitoring of the surfaces of the ring cavity mirrors, as well as the digital methods for processing the initial information, allowing the improvement of the LG accuracy.

2. Ring laser design

The basis of a laser gyroscope is a ring helium–neon laser (Fig. 1). The optical cavity of the laser is formed by spherical

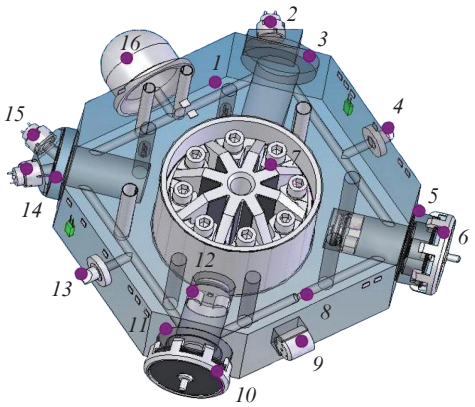

Figure 1. Ring laser design:
(*1*) cavity case; (*2*, *15*) photodetectors; (*3*, *14*) planar mirrors; (*4*) anode; (*5*, *11*) spherical mirrors; (*6*, *10*) piezoelectric correctors; (*7*) vibrosuspension; (*8*) aperture; (*9*) rotor of angular velocity sensor; (*12*) getter pump; (*13*) anode stem; (*16*) cathode.

mirrors (*5*, *11*) with the curvature radii 7.0 ± 0.2 m and transmission coefficients smaller than 5×10^{-6}, and two planar mirrors (*3*, *14*) with the transmission coefficients $(230 \pm 20) \times 10^{-6}$. The optical axis of the cavity is close to the sides of a square with the perimeter 28 cm and is regulated by means of piezoceramic transducers (*6*) and (*10*). The mirror substrates and the cavity case (*1*) are made of CO-115M glass-ceramics and are connected via the optical contact. The choice of optical glass-ceramics is determined by the low coefficient of thermal expansion ($\sim 10^{-7}\,°C^{-1}$) in the range of temperatures from –60 to +80 °C [12].

The laser-generated counterpropagating beams of optical radiation with the wavelength 0.6328 μm have elliptic-shape cross sections and linear s-polarisation (the electric field strength vector being perpendicular to the cavity plane). To provide the oscillation in one fundamental transverse mode only, an aperture (*8*) is placed at the opposite side from the cathode at the beam waist. The elliptic cross section of the aperture fits the shape of the laser beam cross section. The active medium is the mixture of isotopes $^3He:{}^{20}Ne:{}^{22}Ne = 40:1:1$ under the pressure of 750–950 Pa, in which the symmetric bilateral gas discharge is supported with the current of 0.50–0.75 mA in each arm; the discharge channel diameter amounts to 2.7 mm. The use of two isotopes of neon makes it possible to avoid the competition between the counterpropagating waves generated by the laser, which is provided by the difference of 875 MHz between the frequencies, corresponding to the maxima of the gain for the isotopes ^{20}Ne and ^{22}Ne [13].

The directed motion of atoms of the active medium due to the electric current (Langmuir drift) causes the nonreciprocity of counterpropagating waves [14] leading to the shift of the laser gyroscope zero. The use of a symmetric bilateral discharge allows the suppression of this effect; however, the compensation is not complete, which is reflected in the residual systematic error of the zero bias 0.2 deg h^{-1} with the instability 10^{-3}–10^{-2} deg h^{-1}. The ring laser electrodes, two copper anodes (*4*, *13*) placed symmetrically with respect to the cold aluminium cathode (*16*), are connected with the cavity case by means of diffusion melting via an indium gasket. The non-evaporable getter (*12*) made of titanium–vanadium mixture is used to stabilise the working mixture in the course of exploitation.

The phenomenon of locking [15] of the counterpropagating waves generated by the laser is suppressed by means of the forced dithering, the torsional oscillation of the ring laser with respect to the gyroscope case. The resonance frequency of the vibrosuspension (*7*), on which the laser is mounted, amounts to 400 ± 20 Hz. The control system provides the vibrations with the mean amplitude of 120–150″, the amplitude and phase being randomly modulated. The service electronics of the laser gyroscope selects the information about the change in the Sagnac phase, the phase difference between the counterpropagating waves, generated by the ring laser, and also automatically controls the dither frequency and the cavity perimeter, using the signals from the additional sensors: the photodiodes (*15*) for measuring the laser oscillation power and the angular velocity sensor (*9*) that records the vibrations of the ring laser with respect to the gyroscope case.

The simplicity of engineering solutions based on the use of a symmetric direct current discharge and planar cavity, in which the perimeter correction is implemented by microdisplacement of spherical mirrors (*5*, *11*), in combination with close tolerance for the deviation from the shape and linear dimensions, provide a number of advantages of the present scheme as compared to the other schemes of ring lasers, namely:

(i) the sensitivity to the external magnetic field does not exceed 0.002 deg h^{-1} Oe^{-1} (the value so small in comparison with the sensitivity of Zeeman ring lasers [16] is determined by the absence of nonreciprocal elements and the linear polarisation of laser radiation);

(ii) the possibility of tuning the cavity perimeter within six wavelengths of laser radiation in the temperature range from –60 to +60 °C without switching to the adjacent longitudinal mode limits the relative instability of the scale factor (1×10^{-6});

(iii) the weak dependence of the zero bias on the variations in the external temperature is determined by the symmetry of the construction and the choice of optimal tolerances for the cavity geometry; the corresponding temperature coefficient does not exceed 0.001 deg h^{-1} $°C^{-1}$;

(iv) the noise component 0.0015–0.003 deg $h^{-1/2}$, caused by the random modulation of the mecahnical dither, is reduced at the expense of the choice of a four-mirror cavity, as well as using the mirrors with the integral scattering $(10-30) \times 10^{-6}$ and relatively large curvature radius [15];

(v) the small drift instability during the start and from start to start (0.01 deg h^{-1}) is caused by the low level of nonreciprocity at the operational cavity misalignments.

3. Supporting the steady-state bilateral discharge and the problem of the ring laser service life

By choosing the conditions of the ring laser active medium excitation, one should take into account a number of specific features of the discharge in inert gases, consisting in the possible instability of its steady state and in inevitable variations in pressure and composition of the gas mixture due to the ion bombardment of the surface of the cold cathode and the walls of discharge channels. To inhibit the sputtering, the cathode is coated with the oxide film 20–25 nm thick. In comparison with pure aluminium, the film has an increased energy threshold of sputtering and is an efficient emitter of secondary electrons. The long-time maintenance of high emission efficiency of the coating is provided by the helium ion implantation over all its depth [17], which stimulates the photoelectron emission caused by intense absorption of the resonance radiation of helium with the photon energy 21.2 eV [18]. The absorption of vacuum ultraviolet radiation in the oxide layer explains also the experimentally recorded increase in the coating conductivity by three orders of magnitude under the conditions of gas discharge influence [19].

The theoretical description of the gas discharge plasma in a narrow channel [20] is based on the simultaneous solution of the Poisson equation for the electric field and the balance equations for electrons, ions and metastable atoms, taking into account the diffusion and the drift of charged particles across the discharge channel, direct and stepwise ionisation of atoms as a result of collision with electrons, chemoionisation

$$\begin{aligned} He^* + He^* &\rightarrow \begin{cases} He^+ + e + He, \\ He_2^+ + e; \end{cases} \\ Ne^* + Ne^* &\rightarrow \begin{cases} Ne^+ + e + Ne, \\ Ne_2^+ + e; \end{cases} \end{aligned} \qquad (1)$$

and Penning ionisation

$$He^*(Ne^*) + X \rightarrow X^+ + e + He(Ne), \quad (2)$$

where X is the impurity atom (molecule).

The gas discharge plasma in narrow channels, characterised by the near-axis concentrations of electrons $n_e \sim 10^{10}$ cm^{-3} and metastable atoms $n_m \sim 10^{12}$ cm^{-3}, has a falling current–voltage characteristic. Figure 2 illustrates the origin of the negative dynamic resistance. The results of measuring the linear reaction of the positive column to the external harmonic perturbation by means of the technique developed in Ref. [21] are presented in the form of a hodograph of the frequency dependence of its complex impedance. Near the points the values of the modulation frequency in kHz are indicated. The synthesised equivalent electric circuit is also presented here; the resistors and inductors are chosen such that the frequency dependence of the complex impedance reproduces the one recorded experimentally. The inertial elements in the circuit (*RL* circuits) simulate the processes in the positive column, forming the response to the external impact. Since the characteristic times (ratios of L/R) of the inertial elements are strongly different, each of them reflects the influence of a definite process on the ionisation balance.

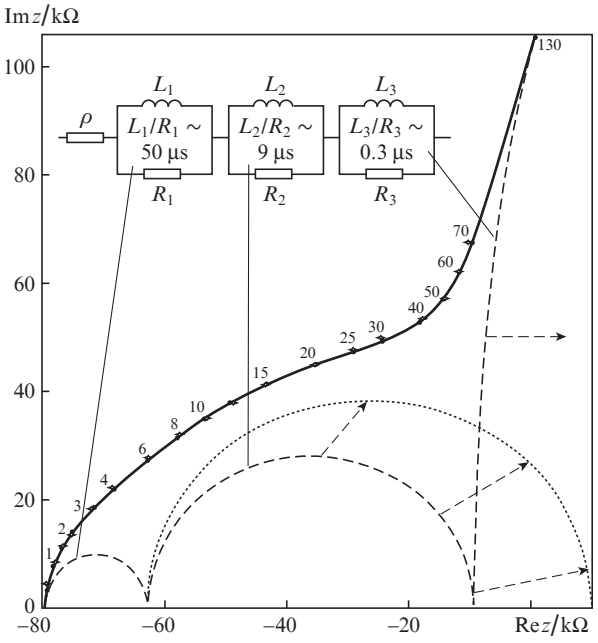

Figure 2. Frequency dependence of complex impedance of the positive column in one of the arms of the ring laser and its equivalent circuit (the current in the arm is 0.75 mA). Every dashed-line semicircle corresponds to the hodograph of only one inertial element of the circuit, the dotted-line semicircle illustrates the change in the hodograph with the growth of the partial pressure of impurities; the figures at the points show the modulation frequency in kHz.

The slowest process is the establishment of the gas concentration distribution between the anode and cathode: the relaxation of the Langmuir drift of atoms is characterised by the time constant $\tau_1 = \Lambda^2 d/\eta \sim 50$ μs ($\Lambda = r_0/2.405$; r_0 is the discharge channel radius; and d and η are the density and viscosity of the gas, respectively). The least inertial is the establishment of electron concentration: $\tau_3 = \Lambda^2/D \approx 0.3$ μs (D is the diffusion coefficient for charged particles under the conditions of transition for the ambipolar regime to the free one). The intermediate value of the time constant τ_2 is a characteristic of the relaxation of the concentration of metastable helium atoms in the state 2^3S_1:

$$\tau_2 = (D_m/\Lambda^2 + 4k_m n_m + k_p N_{ad} + k_e n_e + k_{HeNe} N_{Ne})^{-1}, \quad (3)$$

where D_m is the diffusion coefficient of metastable atoms; k_m, k_p are the rate constants for the processes (1) and (2); N_{ad} and N_{Ne} are the concentrations of impurity and neon atoms in the active medium; and K_{HeNe} is the rate constant of the excitation transfer from helium atoms to neon atoms.

It is of key importance to provide the stability of the boundaries of a narrow 'stability window' of a discharge in the range of current $J_1 > J > J_2$ under the conditions of long-term exploitation. Beyond the 'stability window' at $J > J_1$ the moving striations are self-excited [22], and at $J < J_2$ the reactive oscillations occur [23–25]. The cause of reactive oscillations is the negative real part of the complex impedance of the gas discharge plasma at the frequencies near 100 kHz, when the positive imaginary part of the impedance (see Fig. 2) is compensated by the negative reactive resistance of the wiring capacitance.

A key factor for ring laser technology is the presence of gases (O_2, H_2O, CO_2), diluted in the volume of glass-ceramics that, as a result of ion bombardment of the inner walls of discharge channels, are gradually released into the gas phase and are ionised in reaction (2). The important role of this process for the fixation of the 'stability window' of the discharge is illustrated by Fig. 3: in the plane of parameters 'cathode current J–ballast resistance R' the boundaries of the region of self-excitation of reactive oscillations are shown at different rates of Penning reaction, proportional to the impurity concentration N_{ad}. The increase in the Penning reaction rate in the case of the gas mixture pollution is accompanied with the expansion on the second semicircle in Fig. 2 (shown by arrows). As a result, the real part of the complex impedance in the high-frequency region appears to be positive.

Figure 4 shows the variations of the reactive oscillations threshold J_2 at the initial stage of laser operation. The growth of the reactive oscillation threshold during the first thousand hours is caused by the purification of the helium–neon mixture eliminating the impurities of foreign gases under the action of the gas discharge: the impurities are ionised and brought to the cathode, where they become bound. The achievement of balance between the extraction of foreign gases from the glass-ceramics into the gas volume and their binding at the cathode manifests itself in the stabilisation of the threshold current J_2.

Figure 5 presents the experimental dependence of the cathode current J_{las} corresponding to the double excess of the active medium gain over the losses in the passive cavity on the laser operation time. The growth of J_{las} is caused by the absorption of neon atoms in the process of cathode sputtering; however, after 18 thousand hours its stabilisation occurs.

Figure 6 illustrates the results of the study of the cold cathode surface by means of the atomic-force microscope, showing that the mean square roughness of the coating increases from 1–3 to 15–20 nm under the discharge impact. The roughness growth is due to the nonuniform distribution of the current over the cathode surface because of the focusing of the ion flow by the pores in the oxide coating [26].

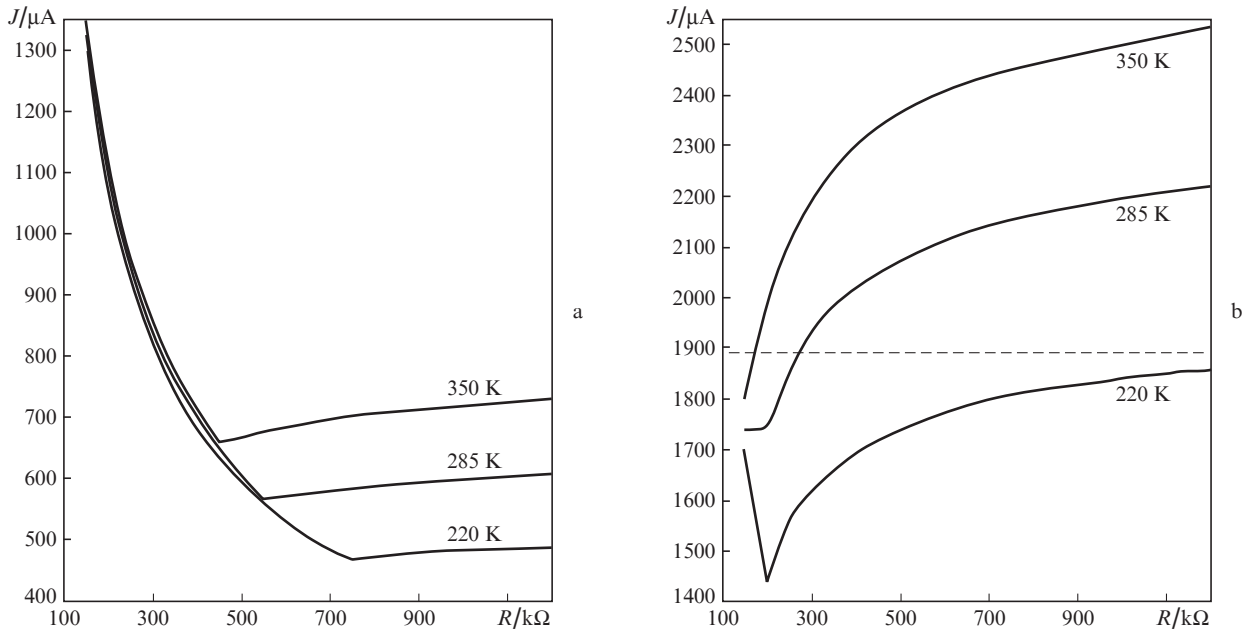

Figure 3. Boundaries of a stable bilateral discharge in the ring laser in the plane of 'cathode current – ballast resistance' parameters. The calculations are performed for the discharge channel with the diameter 2.7 mm; the length of each arm is 63 mm, the pressure of the gaseous filling is 750 Pa, the ratio of components in the mixture is $p_{He}:p_{Ne} = 16:1$ and the wiring capacitance is 2 pF. The solid curves plot the excitation current of reactive oscillations J_2 and the dashed line shows the moving striations arising threshold J_1. The temperatures of the helium – neon mixture are indicated near the curves. The Penning reaction rate is (a) 1.5×10^4 and (b) 1.0×10^3 s^{-1}.

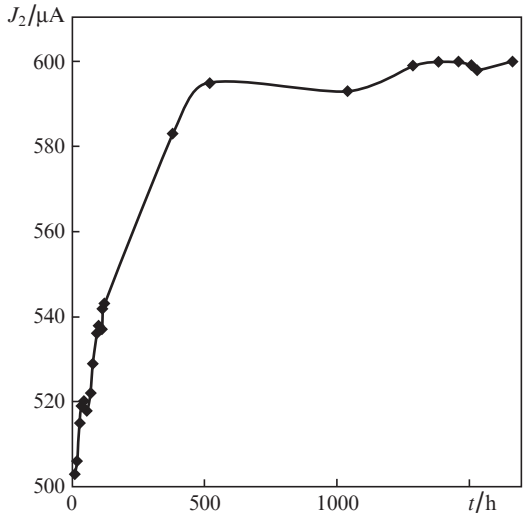

Figure 4. Stabilisation of the reactive oscillation threshold in the discharge electric circuit in the ring laser.

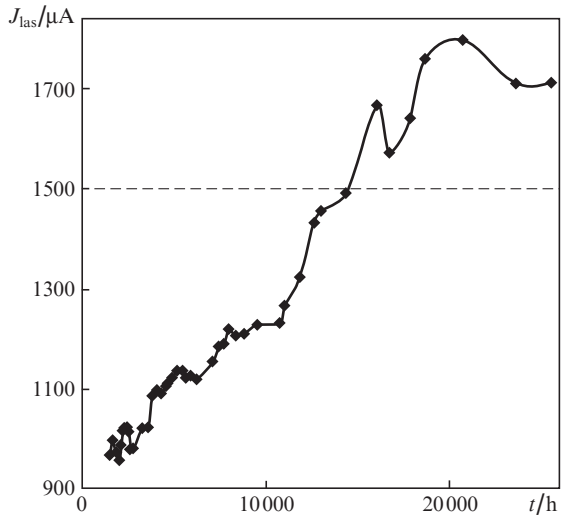

Figure 5. Growth and stabilisation of the current corresponding to double excess of the active medium gain over the losses. The dashed line is the laser operating current.

The long-term conservation of the coating integrity under cathode sputtering is provided by the supply of ionised oxygen atoms from the gas discharge. The formed structure (Fig. 6b) possesses a large effective surface, which allows the neon atoms to return to the gas phase at a rate equal to that of their absorption due to the cathode sputtering. Thus, the direct tests have shown that the technology of ring laser electrovacuum processing, conserving the oxygen within the glass-ceramics volume, provides the service life of 80 thousand hours of continuous operation and stabilises the boundaries of the stability range of the steady-state bilateral discharge. The availability of the obtained results is confirmed by the independent prognosis of the service life time [27] based on the express method of recording the medium degradation rate by the changes of the reaction oscillations characteristics [28].

4. Backscattering of laser radiation in a ring cavity and the characteristic features of the mirror reflecting surface relief

The possibility of measuring small angular velocities with LGs is limited due to the locking of counterpropagating

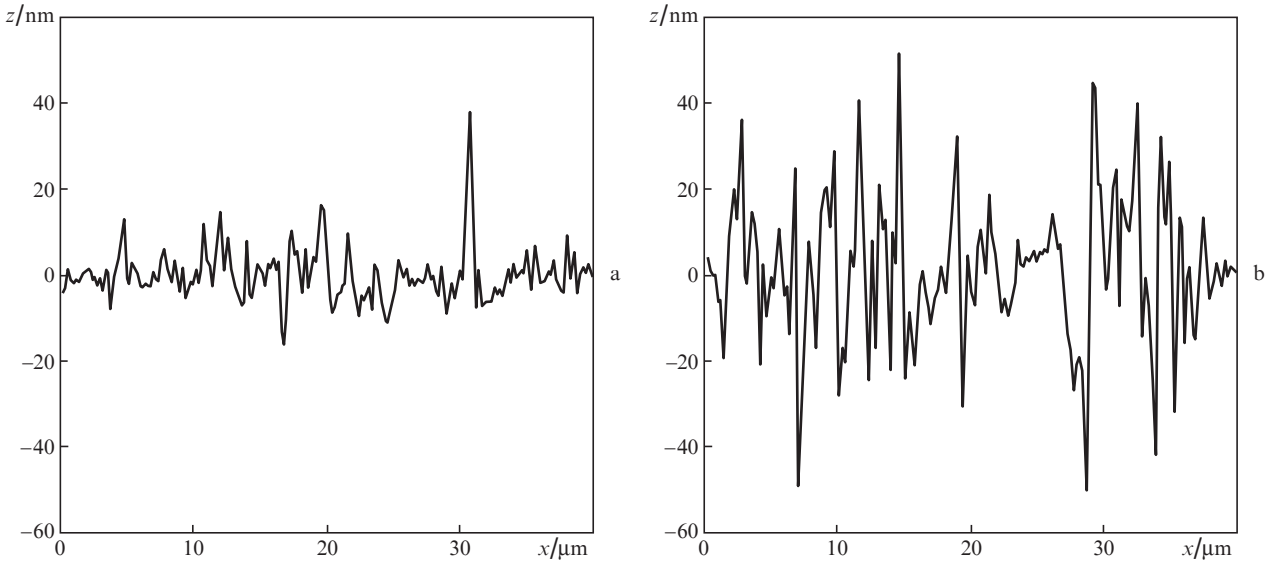

Figure 6. Variations in the surface roughness of the cold cathode made of aluminium with oxide coating as a result of long-term influence of a helium–neon discharge with the current density 0.25 mA cm^{-2}: (a) the initial state after thermal oxidation and (b) after 80000 h of operation. The surface relief is recorded by means of a Solver Pro atomic-force microscope.

waves generated by the ring laser [15]. The origin of this phenomenon is related to the scattering of laser radiation in the direction of the counterpropagating beam by the elements of the ring cavity, the mirrors and the aperture. Until recently, two methods have been used to fight against it, the forced dithering and the improvement of the mirror optical fabrication technology. Quantitatively the locking phenomenon is characterised by the lock-in threshold ω_L, i.e., the maximal angular velocity for which the frequencies of the counterpropagating waves are still equal to each other.

The use of torsional vibrations with a randomly modulated amplitude and phase allows the reduction of the sensitivity threshold of the LG-1 laser gyroscope to 0.02 deg h^{-1} at the lock-in threshold close to 0.03 deg s^{-1}. However, the random modulation of the dithering frequency causes uncertainty of the recorded angular position (angle random walk) and gives rise to a random component in the output signal of the laser gyroscope with the mean square deviation directly proportional to the ratio of the lock-in threshold to the square root of the data averaging time [15].

The radiation backscattering is characterised by the complex amplitude coefficient r, the argument of which is determined by the phases of the scattered waves, and the modulus is given by the relation

$$|r| \approx \sqrt{P_s/P} = \sqrt{I(\theta_0,\theta,\varphi)\,\Delta\Omega}\,, \tag{4}$$

where P_s is the radiation power scattered in the direction of the counterpropagating beam; P is the incident radiation power; $\Delta\Omega = \pi v^2$; $v \sim 10^{-3}$ rad is the divergence of the laser radiation; θ_0 is the angle of incidence; $I(\theta_0,\theta,\varphi)$ is the scattering indicatrix (the ratio of the power, scattered into the unit solid angle, and the power of the incident radiation); and θ and φ are the angles that determine the scattering direction. One should substitute into Eqn (4) the value of the scattering indicatrix in the direction of the counterpropagating beam, i.e., $\theta = \theta_0$.

If the powers of the counterpropagating waves are equal, then the lock-in threshold ω_L in the first approximation is determined by the relation [15, 16]:

$$\omega_L = \frac{c\lambda}{4\pi S}\sqrt{|R_{cw}|^2 + |R_{ccw}|^2 + 2|R_{cw}||R_{ccw}|\cos\Delta\varphi}\,, \tag{5}$$

where c is the velocity of light in vacuum; λ is the laser radiation wavelength; S is the area bounded by the closed contour of the ring cavity optical axis;

$$\begin{aligned} &\Delta\varphi = \arg R_{cw} + \arg R_{ccw}, \\ &R_{cw,ccw} = \sum_{n=1}^{5} r_n \exp(\pm i2kl_{1,n}) \end{aligned} \tag{6}$$

are the amplitude coupling coefficients for the optical waves, propagating clockwise and counter-clockwise [29]; $k = 2\pi/\lambda$; r_n is the complex amplitude coefficient of laser radiation backscattering by the nth element of the cavity; and $l_{1,n}$ is the distance from the scattering element to the base mirror, measured along the optical axis. In the case of a four-mirror cavity (see Fig. 1) there are five scattering elements, the mirrors ($n = 1-4$) and the aperture ($n = 5$).

A more precise presentation of the locking region under the asymmetric coupling of the counterpropagating waves that allows the description of the dependence of its boundaries on not only the complex coupling coefficients of the counterpropagating waves, but also on the active medium gain, is presented in Refs [30, 31]. Equations (6) demonstrate the possibility of changing the coupling coefficients and the lock-in threshold, varying the positions of the scattering elements by displacing the mirror, the cavity perimeter remaining unchanged. The experimental measurements [32, 33], based on weak modulation of the counterpropagating wave power under the variation of Sagnac phase, demonstrate the possibility of choosing such a position of two mirrors, that the lock-in threshold is reduced by several times. The coupling

coefficients can be measured and minimised in the passive ring cavity after its assemblage, as well [34].

It is known [35] that in the absence of absorption and with the scattering centre size much smaller than the wavelength, the arguments of the backscattering amplitude coefficients coincide with the phase difference of a Gaussian beam and a spherical wave ($\pi/2$). In this case the absolute values of the coefficients are equal, and the phase difference is $\Delta\varphi = \pi$. To characterise this situation, the term 'conservative scattering' is used, since, in spite of the coupling of counterpropagating waves due to backscattering, relations (5) and (6) yield the zero value of the lock-in threshold. The measurements carried out with real ring lasers [32, 33] have shown that the phase difference $\Delta\varphi$ differs from π, which is an evidence of 'nonconservative' scattering in real optical cavities.

During a long time either the losses or the presence of scattering centres with the height from tens to hundreds of nanometres on the mirror surface were considered to be the main reasons of 'nonconservative' scattering. A few years ago the methods of atomic-force microscopy (AFM) began to be used for analysing the topography of ultra-smooth dielectric surfaces [36] with the height resolution attaining 0.1 nm and the lateral resolution of a few nanometres. The AFM scan represents the height z of the surface points x, y and carries information about all characteristic features of the relief. Similar information, although with a much worse lateral resolution, can be obtained using a white light interferometer. The comparison of the recorded relief with the results, obtained using the methods, based on the analysis of angular distributions of the X-ray and optical scattered radiation intensity [37, 38], confirmed the correctness of the analysis of the surface scattering properties based on its AFM scanning. The results of experiments and vector theory of laser radiation scattering with the precision dielectric surface [36–41] show that to achieve the required level of backscattering one should polish the substrate, on which the multilayer interference coating is deposited, till the residual mean square roughness no greater than 0.2 nm within the spatial frequency range $0.07-3\ \mu m^{-1}$.

For the commercial manufacturing of mirrors with ultraweak scattering, information about the mean square roughness is not sufficient, because as a result of processing the surface has non-correlated singularities of different origin, including the local inhomogeneities (impurities), linearly structured singularities, such as the traces of the processing instrument or scratches, and the residual chaotic relief.

Polishing reduces the residual chaotic relief, but increases the number of linearly structured defects [42]. Their characteristic feature is the anisotropy of the scattered radiation, depending on the polarisation of the incident optical beam [43]. It is possible to get information about the characteristics of such objects by selecting the anisotropic component of the scattering. The way to greater reliability is to synthesise several images of the relief, each containing mainly one of its characteristic features. This procedure can be implemented using the multiple-scale image analysis [44], based on the application of wavelet expansions. Figure 7 presents the stages of selecting the characteristic features of the AFM image.

The image of the surface region recorded by means of an atomic-force microscope (stage 1) is expanded in fifth-order Daubechies wavelets, and in the expansion the terms corresponding to solitary juts and the scored relief are separated (stage 2). The image of the scored relief is subjected to the Radon transformation that transforms the extended objects

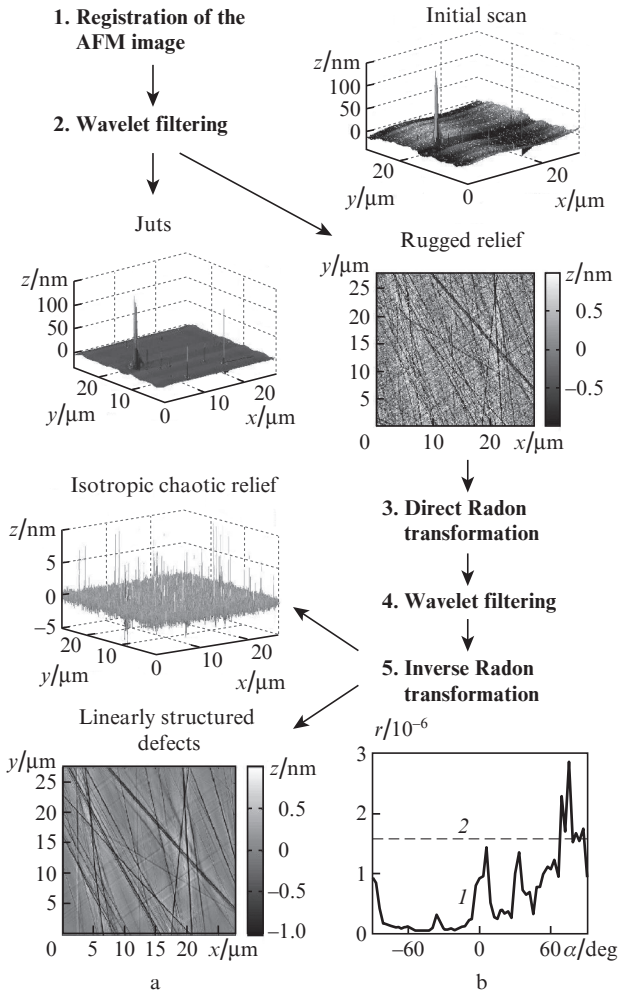

Figure 7. (a) Selection of characteristic features in the AFM image of a region of the optical surface: the synthesis of images of the isotropic chaotic relief and linearly structured defects; (b) dependences of the amplitude backscattering coefficient on the azimuthal orientation of the optical surface [(*1*) scattering from linearly structured defects, (*2*) scattering from isotropic chaotic relief].

oriented along the surface into the solitary juts (stage 3). Wavelet filtration of the juts in the Radon space (stage 4) and the inverse transformation (stage 5) provide the separation of images of linearly structured defects and the isotropic chaotic relief. The coefficients of mutual correlation between the synthesised images of different characteristic topography features of the optical surface do not exceed 0.2, which allows them to be considered statistically independent. The image of linearly structured defects, the traces of mechanical and chemical procession of the surface, are characterised by the scattering indicatrix having pronounced diffraction maxima.

As an illustration of the anisotropy of scattering properties, Fig. 7 presents the dependences of the amplitude coefficient of backscattering on the azimuthal orientation of the optical surface (the angle α), calculated for the linearly structured singularities and the isotropic chaotic relief. The obtained result demonstrates the effect of the procession traces on the amplitude coefficient of backscattering and the necessity to consider them as a significant cause of 'nonconservative' scattering that remains even when the absorption losses are negligibly small. The described method of analysis of mirror scattering properties allows the selection of mirrors

with minimal values of the amplitude coefficient of backscattering from the linearly structure defects and reduces the locking threshold of the counterpropagating waves.

5. Processing of information in a laser gyroscope with high-precision registration of the interference pattern shift

The source of information about the rotation is the variation of the Sagnac phase ψ [15] that causes the displacement of the pattern formed on the surface of the coupling prism (*14*) as a result of the interference of laser beams outcoupled from the ring laser (Fig. 8). The signals at the outputs of the photodiode (*8*), in which the centres of detecting sections are separated by a quarter of the interference fringe width, have the form:

$$U_c(t) = U_{c,0} + U_{c,m}\cos[\psi(t)],$$
$$U_s(t) = U_{s,0} + U_{s,m}\sin[\psi(t) + \gamma], \quad (7)$$

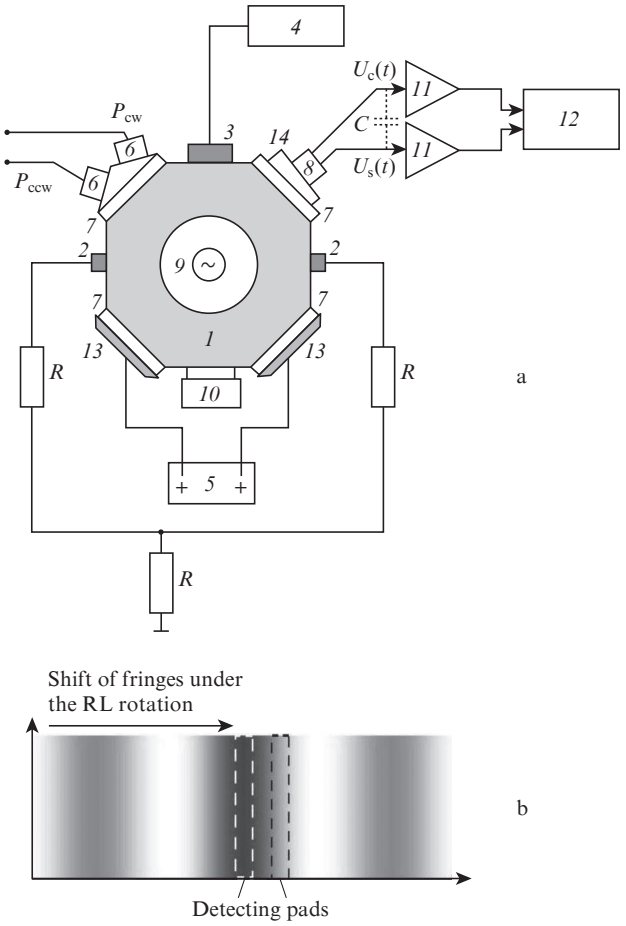

Figure 8. Formation of quadrature signals in the ring laser: (a) the electric scheme of RL and (b) the shift of interference pattern with respect to detecting pads of the sectioned photodiode:
(*1*) glass-ceramic monolithic block; (*2*) anodes; (*3*) cold cathode; (*4*) high-voltage source; (*5*) piezoelectric transducers control unit; (*6*) photodiodes for recording the powers of counterpropagating waves; (*7*) mirrors; (*8*) sectioned photodiode; (*9*) vibrosuspension with a source of variable voltage; (*10*) angular velocity sensor; (*11*) amplifiers of initial signals; (*12*) ADC; (*13*) piezoelectric transducers; (*14*) coupling prism.

where γ is the additional phase shift due to imperfection of the optical system; $U_{c,0}$, $U_{s,0}$ are the constant biases; and $U_{c,m}$ and $U_{s,m}$ are the amplitudes of the quadrature signals. The method of processing the initial signal (7) being in use at present allows the fixation of the Sagnac phase only by the integer multiple of π/n rad ($n = 1-4$) that corresponds to the nominal sensitivity to angular motions $\sim 1''$ [10, 15]. This approach excludes the possibility of obtaining information about the real value of the phase at the moment of picking up the data from the laser gyroscope, which is executed with the rate of 2.0 kHz, and also does not provide total subtraction of the oscillations at the dithering frequency from the output signal.

Figure 9 shows the square root of the Allan variance σ_ω as a function of averaging time T; as the initial information the array of output data from the LG-1 laser gyroscope is used. The counts of angular displacements in this case were executed at time intervals being integer multiples of the dithering period at zero value of the angle (the error of dither subtraction is absent). Lines *1*, *2* and *3* illustrate the contribution of the sources σ_1, σ_2 and σ_3, respectively, each characterised by the specific dependence on the averaging time – the quantisation noise, the noise due to random dithering frequency and the zero shift instability. The known relation between the noise due to random dithering and the lock-in threshold [15] allows the estimation of its value as $\omega_L \approx 0.023$ deg s^{-1}. The theoretical limit for the quantisation noise, the discretisation step of the Sagnac phase being equal to π, typical under the conditions of direct counting of interference fringes, shifted with respect to the detecting pads of the photodiode (*8*) (see Fig. 8) amounts to $1.3\times10^{-4}/T$ deg h^{-1}. The combined effect of all sources is illustrated by line *4* (Fig. 9), plotting the results of direct measurements. Thus, for achieving an acceptable error with the high rate of information update, it is first of all necessary to suppress the quantisation noise by two orders of magnitude.

A promising method is the precision recording of the interference pattern shift [45], used in laser interferometry [46]

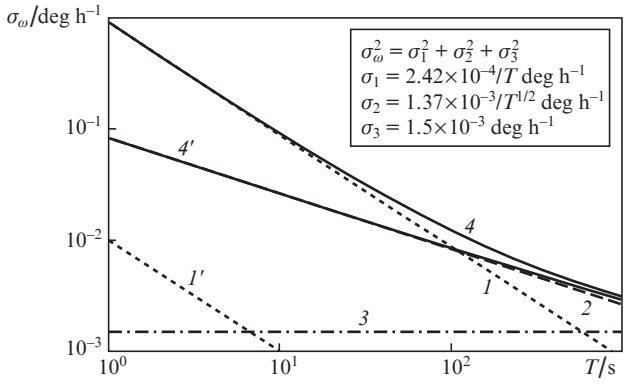

Figure 9. Dependence of the square root of the Allan variance on the averaging time for the LG-1 laser gyroscope:
(*1*) contribution of quantisation noise under the direct counting of interference fringes; (*1′*) contribution of quantisation noise under precision registration of interference patter shift; (*2*) contribution of noise caused by the random dither frequency; (*3*) contribution form the zero shift instability; (*4*) experimentally recorded dependence for the direct counting of interference fringes; (*4′*) square root of the Allan variance for the precision registration of the interference pattern shift. The time T in the formulae for σ_1 and σ_2 is measured in hours.

and including the following stages: discretisation of initial quadrature signals; approximating by an ellipse the set of points corresponding to the digitised region of realisation in the plane of the variables $U_c(t)$ and $U_s(t)$; determination of the parameters of the primary signals (7); and restoration of the time series for the phase difference between the counterpropagating waves.

The implementation of this approach in the laser gyroscope signal processing [47, 48] did not require any information sources, except the signals at the outputs of the sectioned photodetector (*8*), and allowed one to increase the precision of the interference pattern shift recording and to reduce the error of the Sagnac phase measurement to 0.03 rad. When the number of ADC digits is no smaller than 12, the precision is limited by the parasitic capacity coupling between the information channels [49] and the noises of the amplifier of the photodetector signals. As a result, the noise, introduced into the output signal by the errors of registration, is reduced by two orders of magnitude (line *1′* in Fig. 9), and the dominant contribution to the value of the random error is introduced by the random dither frequency (line *4′*).

The potential capabilities of the precision method of processing the laser gyroscope signal allow the following:

(i) recording the variations of the phase difference between the counterpropagating waves, generated by the ring laser, having the value of a few hundredths of radian, which corresponds to the sensitivity to the angular displacements of the order of 0.01″;

(ii) increasing the rate of updating the output information about the angular motions to 10 kHz;

(iii) adapting automatically the laser gyroscope to the changing conditions of its operation;

(iv) suppressing the oscillations at the dither frequency in the output signal of the laser gyroscope by means of the digital rejection filter; and

(v) making the auxiliary photodiodes (*6*) (see Fig. 8) unnecessary, since the amplitudes of the quadrature signals $U_{c,m}$, $U_{s,m}$, are proportional to the laser oscillation power.

The elliptical filter [50] provides the combination of the required operation rate with the acceptable delay of the output signal. Figure 10 shows the distortions of the test signal at the output of such a filter and the dependence of the error arising in the course of uniformly accelerated rotation of the RL by the angle 10° on the angular acceleration. The advantage of this method of data processing is the practically complete subtraction of the dither frequency from the LG output signal.

In the SINS mathematical model, information from the laser gyroscopes was subjected to processing using the method of Sagnac phase time series reconstruction. As the initial data for the study of dynamic capabilities of the laser gyroscope output information processing method the real trajectories obtained during the flight test of the SINS aboard the Yak-130 aircraft were used.

Figure 11 presents the results of modelling of the information signal selection process in the course of digital processing and rejection filtering of the raw data from the laser gyroscope used in the list sensing channel for the fragment of a 400-s-long flight. To remove the dither, the elliptical filter of the 10th order with the 60 dB attenuation in the frequency band 5 Hz was used. The trajectory motions consist of combinations of fast manoeuvres with the angular accelerations approaching 1000 deg s^{-2}, to which the short-time spikes of the reconstructed angle error up to 10–12″ correspond. The reconstructed angle error oscillates about the zero mean value and is not accumulated.

When implementing this information processing method, some LG elements, presently in use (see Fig. 1), become superfluous, namely, the angular velocity sensor (*9*) and the photodiodes (*15*) at one of the planar mirrors (*14*), the reflection coefficient of which can be reduced from 230×10^{-6} to 5×10^{-6}. The elimination of excess sensors will allow the elimination of the appropriate units of service electronics.

Thus, the possibility of efficient suppression of quantisation noises of the laser gyroscope and the stability of the processing method with respect to dynamic trajectory motions of the object are demonstrated. The obtained results confirm the reasonability of using the registration of the interference pattern motion in real time [44] with the aim of determining the Sagnac phase variation by the counts of the raw quadrature signals of the laser gyroscope in autonomous SINS's for aircraft application.

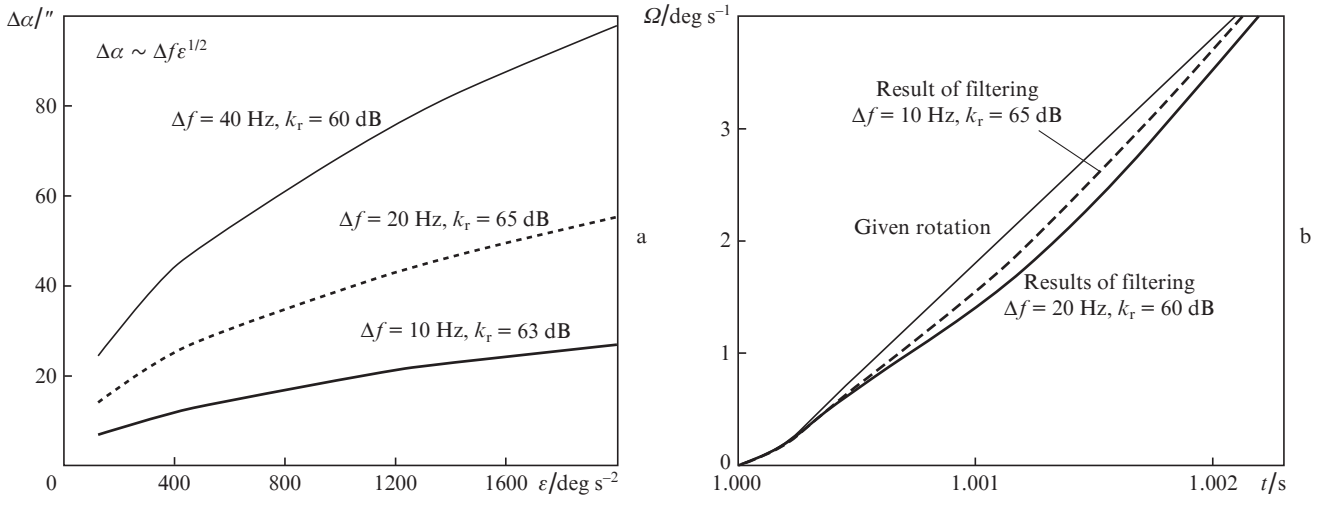

Figure 10. Dependences of LG systematic error on the angular acceleration ε under the rotation by the angle of 10° (a) and the output signal under the uniformly accelerated rotation (b). The suppression bands Δf and the suppression coefficients k_r of elliptic filters are indicated.

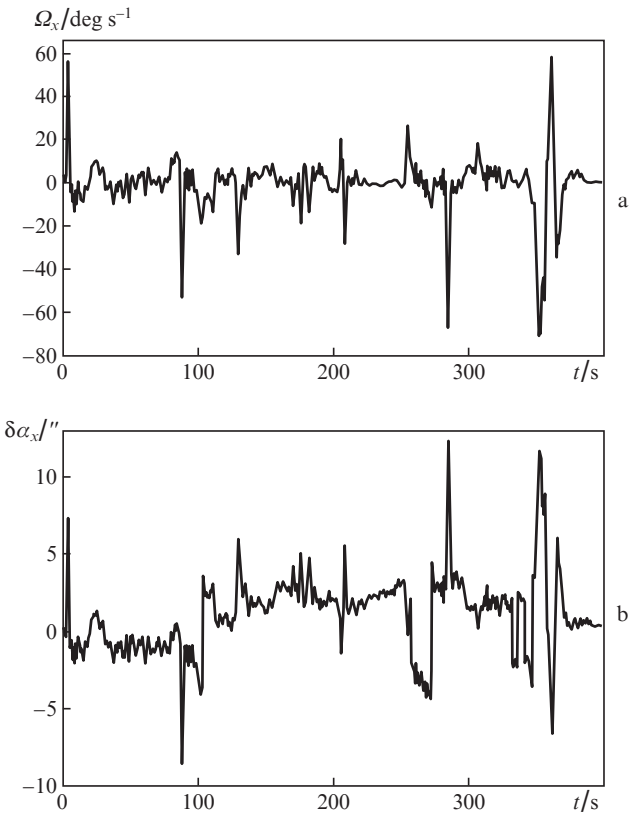

Figure 11. (a) Angular velocities recorded with the laser gyroscope used as the list angle sensor and (b) the errors of the list angle reconstruction after the dither filtering.

6. Conclusions

1. The physical mechanisms that determine the stability of the discharge and the gas exchange processes in a ring laser are considered. The results, including those obtained in the direct tests, show that the service life of a ring laser with a cold cathode is determined by the combination of degradation and restoration processes that occur in the direct-current discharge. The found regularity allows the formation of conditions that provide the prescribed service life time of a ring laser.

2. The application of the described methods of recording AFM images of small-scattering mirrors and their substrates, as well as the methods of processing these images aimed at revealing the characteristic features of their relief allow:

– selection of the mirrors and mirror substrates with minimal scattering by the linearly structured singularities that remain after polishing, and reduction of 'nonconservative' scattering in the ring cavity;

– selection and classification of mirror and substrate defects, and, as a consequence, the information needed to control the technology of mirror fabrication.

3. It is shown that the considered method of Sagnac phase extraction from the raw quadrature LG signals allows:

– efficient suppression not only of the noise caused by incomplete dither subtraction, but also of that caused by quantisation;

– essential increase in the LG output information updating rate, which is necessary for increasing the precision, particularly, in the case of highly dynamical objects;

– the required quality of the output LG information to be provided during the highly dynamical motion of the object;

– simplification of the LG construction.

References

1. http://www.aerospace.honeywell.com./guidance-sensor-inertial-products.
2. http://www.usd.es.nortropgrumman/com.
3. http://www/sagem-ds/com.
4. Peshekhonov V.G. *Giroskopiya i navigatsiya*, (1), 3 (2011) [*Gyroscopy and Navigation*, **2**, 111 (2011)].
5. Kuznetsov A.G., Izmaylov E.A. *Trudy FGUP 'NPTs AP'. Sistemy i pribory upravleniya*, (1), 3 (2012).
6. Linch D. *Giroskopiya i navigatsiya*, (3), 102 (2008).
7. Sukhanov S.V. *Datchiki i sistemy*, (11), 20 (2009).
8. Izmaylov E.A. *Trudy FGUP 'NPTs AP'. Sistemy i pribory upravleniya*, (1), 30 (2010).
9. Kryukov S.P., Chesnokov G.I., Troitskiy V.A. *Proc. 9th Intern. Conf. Integrated Navigation Systems* (St. Petersburg, Russia, 2002) p. 343.
10. Chesnokov G.I., Polikovsky E.F., Molchanov A.V., Kremer V.I. *Proc. 10th Intern. Conf. Integrated Navigation Systems* (St. Petersburg, 2003) p. 277.
11. GOST RV 52 339-2005. *Sistemy besplatformennye inertsialno-navigatsionnye na lasernykh giroskopakh* (Russian State Military Standard 52 339-2005. Lager Gyroscope Based Strapdown Inertial Navigation Systems) (Moscow, 2005) p. 15.
12. Buzhinskii I.M., Zhukovets Zh.G. *Metrologiya*, (9), 38 (1986).
13. Aronowitz F. *The laser gyro*. In: *Laser Applications* (Ed. by M. Ross) (New York: Academic Press, 1971; Moscow: Mir, 1974).
14. Kravtsov N.V., Kravtsov N.N. *Kvantovaya Elektron.*, **27**, 98 (1999) [*Quantum Electron.*, **29** (5), 378 (1999)].
15. Aronowitz F., in *Optical Gyros and Their Application* (Hull, Quebec, Canada: Canada Commun. Group Inc., 1999) p. 3-1.
16. Azarova V.V., Golyaev Yu.D., Dmitriev V.G. *Kvantovaya Elektron.*, **30**, 96 (2000) [*Quantum Electron.*, **30**, 96 (2000)].
17. Nikiforov D.K., Korzhavyi A.P., Nikiforov K.G., Bondarenko G.G. *Izv. Vyssh. Uchebn. Zaved., Ser. Fiz.*, **56**, 23 (2013).
18. Bokhan P.A., Zakrevskii D.E. *Zh. Tekh. Fiz.*, **77**, 109 (2007) [*Tech. Phys.*, **52** (1), 104 (2007)].
19. Kryutchenko O.N., Mannanov A.F., Nosov A.A., Stepanov V.A., Chirkin M.V. *Poverkhnost', Fizika, Khimiya, Mekhanika*, (6), 93 (1994).
20. Morozov D.A., Stepanov V.A., Chirkin M.V. *Izv. Ross. Akad. Nauk, Ser. Fiz.*, **64**, 126 (2000).
21. Aleksandrov L.S., Perebyakin V.A., Stepanov V.A., Chirkin M.V. *Fiz. Plazmy*, **15**, 467 (1989).
22. Zakharov M.A., Molchanov M.I., Yaroshenko N.G. *Radiotekh. Elektron.*, **29**, 2403 (1984).
23. Chetverikov V.I. *Radiotekh. Elektron.*, **31**, 108 (1986).
24. Udal'tsov B.V., Tsar'kov V.A. *Radiotekh. Elektron.*, **31**, 938 (1986).
25. Mazan'ko I.P., Udal'tsov B.V., Tsar'kov V.A. *Radiotekh. Elektron.*, **31**, 2042 (1986).
26. Kryutchenko O.N., Mannanov A.F., Nosov A.A., Stepanov V.A., Chirkin M.V. *Radiotekh. Elektron.*, **41**, 990 (1996).
27. Chirkin M.V., Molchanov A.V., Morozov D.A., Osetrov I.V. *Proc. XV Int. Conf. on Gas Discharges and their Applications* (Toulouse, France, 2004) Vol. 1, p. 447.
28. Molchanov A.V., Morozov D.A., Osetrov I.V., Sauridi A.G., Chirkin M.V. RF Patent No. 2402833, priority of 20.05.2009.
29. Rodloff R. *IEEE J. Quantum Electron.*, **QE-23**, 438 (1987).
30. Bondarenko E.A. *Kvantovaya Elektron.*, **41**, 824 (2011) [*Quantum Electron.*, **41**, 824 (2011)].
31. Bondarenko E.A. *Kvantovaya Elektron.*, **42**, 465 (2012) [*Quantum Electron.*, **42**, 465 (2012)].
32. Molchanov A.V., Stepanov A.Yu., Chirkin M.V. *Aviakosmicheskoye priborostroyeniye*, (3), 9 (2008).
33. Dovbeshko A.A., Pavlovskii M.A. *Giroskopiya i navigatsiya*, (1), 27 (1995).
34. Krenz G., Bux S., Slama S., Zimmermann C., Courteille P.W. *Appl. Phys. B*, **87**, 643 (2007).

35. Haus H.A., Statz H., Smith I.W. *IEEE J. Quantum Electron.*, **QE-21**, 78 (1985).
36. Zanaveskin M.L., Roshchin B.S., Grishchenko Yu.V., Azarova V.V., Asadchikov V.E., Tolstikhina A.L. *Kristallograf.*, **33**, 740 (2008) [*Crystallography Reports*, **53**, 701 (2008)].
37. Zanaveskin M.L., Zanaveskina I.S., Roshchin B.S., Asadchikov V.E., Grishchenko Yu.V., Tolstikhina A.L. *Vestnik Moskovskogo Univer., Ser. Fiz., Astronom.*, (3), 80 (2006).
38. Azarova V.V., Dmitriev V.G., Lokhov Yu.N., Malitskii K.N. *Opt. Zh.*, **69**, 71 (2002).
39. Azarova V.V., Dmitriev V.G., Lokhov Yu.N., Malitskii K.N. *Kvantovaya Elektron.*, **30**, 360 (2000) [*Quantum Electron.*, **30**, 360 (2000)].
40. Azarova V.V., Dmitriev V.G., Lokhov Yu.N., Malitskii K.N. *Kvantovaya Elektron.*, **31**, 740 (2001) [*Quantum Electron.*, **31**, 740 (2001)].
41. Gomes-Rosas G., Malacara-Hernandes D., Wang H. *Opt. Quantum Electron.*, **32**, 63 (2000).
42. Wang H. *Opt. Laser Technol.*, **26**, 333 (1994).
43. Germer T.A. *J. Opt. Soc. Am. A*, **24**, 696 (2007).
44. Chirkin M.V., Molchanov A.V., Serebryakov A.E. *Proc. 5th Intern. Conf. 'Optical Measurement Techniques for Structures and Systems'* (Antwerp, Belgium, 2012) p. 93.
45. Zumberge M.A., Berger M.A., Dzieciuch M.A., Parker R.L. *Appl. Opt.*, **43**, 771 (2004).
46. Pozar T., Mozina J. *Meas. Sci. Technol.*, **22**, 085301 (2011).
47. Alekseev S.Yu., Borisov M.V., Zakharov M.A., Mishin V.Yu., Molchanov A.V., Morozov D.A., Chirkin M.V. *Radiotekh.*, (3), 165 (2012).
48. Alekseev S.Yu., Borisov M.V., Zakharov M.A., Mishin V.Yu., Molchanov A.V., Morozov D.A., Chirkin M.V. *Giroskopiya i navigatsiya*, (2), 75 (2013) [*Gyroscopy and Navigation*, **4**, 223 (2013)].
49. Chirkin M.V., Mishin V.Yu., Molchanov A.V., Morozov D.A. *Proc. 18th Intern. Conf. Integrated Navigation Systems* (St. Petersburg, Russia, 2001) p. 48.
50. Lutovac M.D., Tosic D.V., Evans B.L. *Filter Design for Signal Processing using MATLAB and Mathematica* (NJ, USA: Prentice Hall, 2001).